**GEOLOGICAL CHARACTERISTICS OF CHANG'E-4 LANDING SITE.** Jun Huang[1], Zhiyong Xiao[1], Jessica Flahaut[2], Mélissa Martinot[3,4], Xiao Xiao[1], [1]Planetary Science Institute, China University of Geosciences (Wuhan) (junhuang@cug.edu.cn), [2]IRAP Université Paul Sabatier, 31400 Toulouse, France, [3]Vrije Universiteit Amsterdam, 1081HV Amsterdam, The Netherlands, [4]LGL-TPE University of Lyon, 69622 Villeurbanne cedex, France

**Introduction:** China plans to send Chang'E-4 (CE-4) to the South Pole-Aiken (SPA) basin for in-situ exploration [1]. CE-4 will be the first in-situ exploration for the far side of the moon if it succeeds. The mission will be carried out in two steps. Firstly, a relay satellite with two micro satellites will be launched by a CZ-4C rocket in Xichang, China. The relay satellite, equipped with a low-frequency radio spectrometer (developed in the Netherlands), will be sent to the Earth-Moon Lagrange Point 2 to make unique space physics measurements. In addition, there will be laser reflectors for orbital determination assistance and technic experiments. The two micro satellites will be equipped with Very-long-baseline interferometry (VLBI) and micro visible cameras contributed from Saudi Arabia. Six months later, the second part of CE-4, a lander and a rover, will be launched by CZ-3B rocket from Xichang, China. Since the lander and rover were designed as the backup of the Chang'E-3 mission, there are several similar scientific payloads including Landing Camera, Topographic Camera on the lander, and Panorama Camera, Visible/Near Infrared Imaging Spectrometer, Ground Penetrating Radar on the rover. The additional instruments are Low-Frequency Radio Spectrometer, Lunar Neutron and Radiation Dose Detector (developed in Germany), and Lunar Micro Ecosystem on the lander, and Neutral Atom Detector (developed in Sweden) on the rover. It is will very important to propose targets of high scientific interests for Chang'E 4 mission, so we present geological characteristics of the candidate landing site in this study.

The candidate landing region is 45°S-46°S 176.4°E-178.8°E, which is in the southern floor of the Von Kármán crater, within the SPA basin (Fig. 1a). Von Kármán is a pre-Nectarian crater of 180 km in diameter [2]. Mare basalt flows filled the crater floor subsequently at ~3.35 Ga [3], but a portion of possible central peak remains near the center of the crater (Fig. 1b). NRC [4] has previously identified goals for future sample return mission in Von Kármán crater, including the possibility to study the existence and extent of differentiation of the SPA melt sheet and possible exposed upper mantle materials.

**Data and Methods:** We analyzed the topography of the candidate landing region using the Lunar Reconnaissance Orbiter (LRO) Lunar Orbiter Laser Altimeter (LOLA) and Kaguya Terrain Camera (TC) merged Digital Elevation Modal (DEM) [5], the spatial sampling is 512 ppd (59 m/pix). Spectral analyses were performed using the Kaguya Multiband Imager (MI) and Chandrayaan-1 Moon Mineralogy Mapper (M3) data. Geomorphologic characteristics were studied with LRO Wide Angle Camera (WAC), Narrow Angle Camera (NAC), and TC images.

**Results:** The candidate landing region within Von Kármán crater is generally flat in the DEM. The northeastern and southwestern portions are relatively lower while the northwestern and southeastern portions are relatively higher in altitude. The average altitude in this area is about -5926 m, with a standard deviation of 20.4 m. The elevation range is about 321 m. Nearly 99% of the area has a slope inferior to 15°, and the slopes of about 94% of the area is inferior to 5° at a 59 m scale. The steepest slopes of the region occur on the walls of craters (both primary and secondary ones) and the only butte in the region.

The estimated thickness of regolith in this area varies from 2.53 m to 7.49 m based on available LROC NAC images (incidence angle inferior to 55°). It appears that the regolith in the northeastern part is thicker than that of the southwestern part.

We have identified spectral variations in the MI RGB composite (Fig. 2b) and $M^3$ VNIR spectra, especially around impact craters within the mare which expose fresher materials. Smaller craters (diameter 66 – 324 m) show blue toned ejecta (higher albedo in the MI 750 nm reflectance data) and present spectra close to Low-Calcium Pyroxene (LCP)-bearing materials (Fig. 2b and 2c). The orange toned ejecta are related to larger craters (diameter 252 – 950 m), with spectra closer to High-Calcium Pyroxene (HCP)-bearing materials (Fig. 2b and 2c). The ejecta on the rim of the largest crater near the landing region presents HCP signature, but larger spectral contrast. The mare itself has a spectral signature closer to these HCP-rich material with weaker bands as it was exposed to space weathering for a longer time period.

Secondary craters occur all over the candidate landing region (Fig. 1c). We have identified at least two source craters (Finsen and Antonadi) for these secondary craters. The secondary craters observed on the mare in Von Kármán crater floor have a diameter inferior to 2 km , therefore, we measured craters larger than 2 km for crater size frequency distribution measurements. The absolute model age is 3.6 (+.09, -.2) Ga, which falls in the Imbrium age.

Interestingly, we have identified many sinuous ridges within the candidate landing region. The ridges are asymmetric in shape and stretch in a sinusoidal-like shape, and the widths of the ridges are tens of meters. Sinuous troughs are formed between ridges, and both the troughs and ridges are associated with a fresh crater ~4 km diameter to the west of the landing region.

**Discussion:** The different spectra of ejecta related to various sizes of crater reveal vertical composition changes. If we assume the crater depth and diameter ratio is 1/10, then we can estimate the depths of origin of the LCP and HCP bearing materials are comprised between 6.6 – 32.4 m and 25.2 – 95 m, respectively. Therefore, the LCP and HCP-bearing materials are not evenly distributed, although the latter is generally observed deeper in the stratigraphy. Within the HCP layer, we can tell the vertical compositional differences by the different spectral contrast. The deeper portion of the HCP layer has larger absorption band depth than the shallower portion of the HCP layer.

The surficial LCP-bearing material have high albedo (Fig. 2a), and are forming streaks aligned towards Finsen crater (northeast of Von Kármán). It is likely that the LCP-bearing material are part of the ejecta of the Finsen crater forming event. LCP were detected at several locations within SPA basin, including the central peak of Finsen Crater [6]. A recent study [7] has proposed a LCP-dominated upper mantle for the Moon. Alternatively, the LCP-bearing material could correspond to exposed KREEP-related Mg-suite rocks [8,9] or SPA melt sheet [10,11]. The Chang'E 4 rover in-situ measurements could help constraining the composition and origin of the LCP-bearing materials and understanding the stratigraphic relationship between the LCP and HCP-bearing materials. These LCP-bearing materials could help to better constrain the history of the SPA region and might represent high priority targets for future sample return missions, e.g. Chang'E-6.

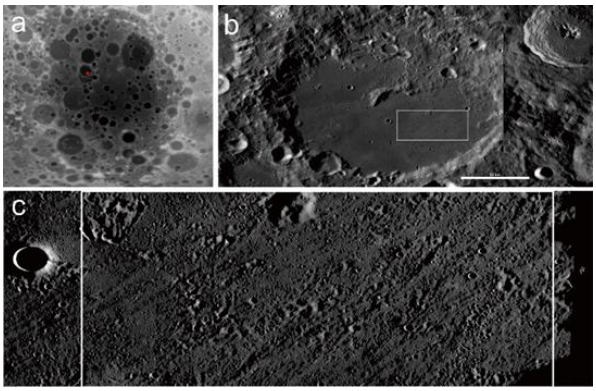


Fig.1 a) The red star indicates the candidate landing region within Von Kármán crater in SPA basin (Background = LOLA topography). b) Context of candidate landing region in the southern portion of Von Kármán crater floor. (LROC WAC mosaic). c) TC morning mosaic of the landing region shown in b; a large number of secondary craters can be observed.

**References:** [1] Wu, W.R., et al., (2017) Journal of Deep Space Exploration, 4(2): p. 111-117. [2] Losiak, A., et al., (2009) Lunar and Planetary Science Conference. [3]Haruyama, J., et al., (2009) Science, 323(5916): p. 905-8. [4] National Research Council, (2007): National Academies Press. [5] Barker, M., et al., (2016) Icarus, 273: p. 346-355. [6] Moriaty et al., (2013) JGR, 118: p. 2310-2322. [7] Melosh, H., et al., (2017) Geology, 45(12): p. 1063-1066. [8] Pieters C.M. et al., (1997) GRL, 24: p. 1903-1906. [9] Klima R.L. et al., (2011) JGR, 116. [10] Nakamura R. et al., (2009) GRL, 36. [11] Uemoto K. (2017) JGR, 122: 1672-1686. [12] Martinot et al., (2018) JGR, 123, 1–18.

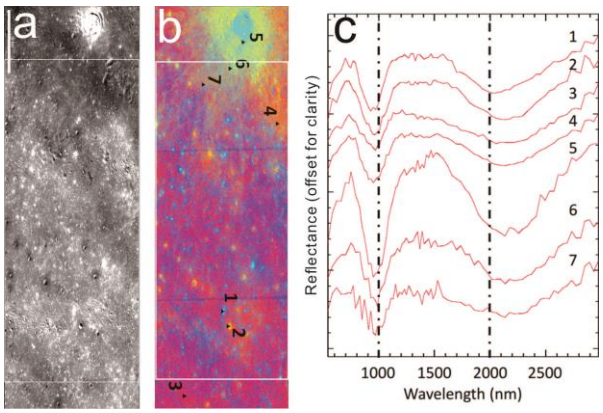


Fig. 2 a) Different albedo features in MI 750 nm reflectance mosaic. b) Different spectral units in MI RGB composite, R: r750/r415 (stretched range: 1.797-1.925), G: r950/r750 (stretched range: 0.877- 1.034), B: r415/r750 (stretched range: 0.515 – 0.564). Numbers indicate the locations of the spectra shown in c. c) Associated $M^3$ continuum-removed spectra, which show pyroxenes signatures (see method in [12]).